

12

ADA 127379

HDL-CR-83-072-1

February 1983

Techniques for Source-Region EMP
Experiments at AURORA

by V. A. J. van Lint

Prepared by

Mission Research Corporation
735 State Street
Post Office Drawer 719
Santa Barbara, CA 93102

Under contract

DAAK21-80-R-9072



U.S. Army Electronics Research
and Development Command
Harry Diamond Laboratories

Adelphi, MD 20783

DTIC FILE COPY

Approved for public release; distribution unlimited.

DTIC
ELECTE
APR 27 1983
E

83 04 26 106

UNCLASSIFIED

SECURITY CLASSIFICATION OF THIS PAGE (When Data Entered)

REPORT DOCUMENTATION PAGE		READ INSTRUCTIONS BEFORE COMPLETING FORM
1. REPORT NUMBER HDL-CR-83-072-1	2. GOVT ACCESSION NO. AD-A127379	3. RECIPIENT'S CATALOG NUMBER
4. TITLE (and Subtitle) Techniques for Source-Region EMP Experiments at AURORA		5. TYPE OF REPORT & PERIOD COVERED Contractor Report
7. AUTHOR(s) V. A. J. van Lint HDL Contact: William Scharf		6. PERFORMING ORG. REPORT NUMBER AURORA EMP Memo 22
9. PERFORMING ORGANIZATION NAME AND ADDRESS Mission Research Corporation 735 State Street Santa Barbara, CA 93102		8. CONTRACT OR GRANT NUMBER(s) DAAK21-80-R-9072
11. CONTROLLING OFFICE NAME AND ADDRESS Harry Diamond Laboratories 2800 Powder Mill Road Adelphi, MD 20783		10. PROGRAM ELEMENT, PROJECT, TASK AREA & WORK UNIT NUMBERS Program Element: 62120A DA Project: 1L162120AH25
14. MONITORING AGENCY NAME & ADDRESS (if different from Controlling Office)		12. REPORT DATE February 1983
		13. NUMBER OF PAGES 35
		15. SECURITY CLASS. (of this report) UNCLASSIFIED
		16a. DECLASSIFICATION/DOWNGRADING SCHEDULE
18. DISTRIBUTION STATEMENT (of this Report) Approved for public release; distribution unlimited.		
17. DISTRIBUTION STATEMENT (of the abstract entered in Block 20, if different from Report)		
19. SUPPLEMENTARY NOTES HDL project: X750E7 DROMS Code: 612120H250011		
20. KEY WORDS (Continue on reverse side if necessary and identify by block number) SREMP Radiation AURORA Nuclear effects Flash x ray		
21. ABSTRACT (Continue on reverse side if necessary and identify by block number) This memo describes reliable measurement techniques for determining source-region EMP parameters in the AURORA room. The general principles involved in each measurement, the interference effects, and specific design considerations for the AURORA environment are discussed. These measurements include the determination of the electromagnetic fields, the current densities, the air conductivity and the induced currents on a conductor. The interference effects, as they relate to each of these measurements, occurring from Compton transfer currents, ionization-induced conduction, shield currents and photo-induced cable currents are also discussed.		

DD FORM 1073 EDITION OF 1 NOV 65 IS OBSOLETE

UNCLASSIFIED

SECURITY CLASSIFICATION OF THIS PAGE (When Data Entered)

CONTENTS

	<u>Page</u>
1. INTRODUCTION	5
2. INTERFERENCES	5
2.1 Compton Transfer Currents	5
2.2 Ionization-Induced Conduction	6
2.3 Shield Currents	7
2.4 Photon-Induced Cable Current	8
3. ELECTRIC FIELD AND VOLTAGE MEASUREMENTS	10
3.1 Potential Difference Technique	10
3.2 Other Methods of Electric Field Measurement	15
3.3 Voltage Measurement	16
4. MEASUREMENTS OF MAGNETIC FIELDS AND CURRENTS	16
4.1 Magnetic Field Measurements	16
4.2 Surface Current Measurement	20
4.3 Volume Current Density	21
4.4 Measurement of Current in a Conductor	23
4.4.1 Current Probe	23
4.4.2 Series Resistor	28
5. MEASUREMENT OF AIR CONDUCTIVITY	28
5.1 Parallel Plate Ionization Chamber	28
5.2 Microwave Absorption and Scattering	31
REFERENCES	32
DISTRIBUTION	33

FIGURES

1. Comparison of Z_T values of various cables	9
2. Electric field sensor	12
3. Magnetic field sensor	18
4. Volume current density sensor	22
5. Current probe	24
6. Schematic diagram of the "pie pan" experiment	29

TABLES

1. Typical Photon-Induced Cable Currents	10
2. Current Probe Specifications	27

1. INTRODUCTION

This report describes reliable measurement techniques for source-region EMP parameter measurements in the AURORA exposure room. Most of these techniques were applied during the course of MRC's support of HDL experiments under contracts DAAG-39-78-C-0026 and DAAG-77-C-0033.

General considerations for interferences in AURORA experiments are described in section 2. Different classes of measurements are described in sections 3, 4, and 5. The general principles of each measurement are followed by interference considerations and specific design examples for AURORA applications.

2. INTERFERENCES

Interferences (caused by energetic radiation, resulting electromagnetic fields and currents) are a pervasive concern in the AURORA exposure room.

The interferences can be classed as: Compton transfer currents, ionization-induced conduction, shield currents, and photon-induced cable currents. Each of the above interferences are discussed below.

2.1 Compton Transfer Currents

The AURORA generated bremsstrahlung photon field is accompanied by a current of Compton electrons whose density is approximately described by

5



Accession For	
NTIS GR&I	<input checked="" type="checkbox"/>
DTIC TAB	<input type="checkbox"/>
Unannounced	<input type="checkbox"/>
Justification	
By	
Distribution/	
Availability Codes	
Dist	Avail and/or Special
A	

$$J_c = K_c \dot{D} \quad (1)$$

where $K_c \approx 2 \times 10^{-8}$ (C/rad m²), and \dot{D} is the dose rate in rads(air)/s. The Compton electrons are created by photon-matter interactions and are continuously slowed down by ionizing collisions. While the equilibrium current density is almost independent of material, objects placed in the photon field can accumulate a net charge. A net charge occurs because of the photon field attenuation passing through the object, electron scattering at interfaces, and the small dependence of Compton current on atomic number.

The fractional imbalance from photon attenuation is described approximately by

$$f \approx 1 - e^{-X/40 \text{ g/cm}^2} \quad (2)$$

where X is the mass density of the object along the photon path.

Contributions from electron scattering and the dependence on atomic number increase slowly with difference in atomic number. The increase is approximately proportional to the mass density, up to the electron range ($\sim 0.3 \text{ g/cm}^2$). For layers thick compared to the electron range, the net current can be up to approximately 20 percent of the Compton current generated within an electron range for large differences in atomic number.

2.2 Ionization-Induced Conduction

All materials exhibit enhanced conductivity while exposed to ionizing radiation. A major area of concern is increased currents across reverse-biased semiconductor junctions. This enhanced collector-base leakage current or reverse-biased diode leakage current is commonly called its primary photocurrent, I_{pp} . The magnitude can be described by

$$I_{pp} = K_{pp} \dot{D} \quad (3)$$

where K_{pp} varies upward by several orders of magnitude from $\sim 10^{-12}$ C/rad for low power (~ 0.25 W) high-frequency devices ($f_T > 100$ MHz), and \dot{D} is the dose rate in rad(Si)/s.

Air is also a conductor in an ionizing field. It's conductivity in the presence of ionizing radiation is given by

$$\sigma = K_G \dot{D} \quad (4)$$

where $K_G \approx 3 \times 10^{-11}$ mho s/rad m (approximate value for damp air),¹ and \dot{D} is the dose rate. The conductance across an air gap between conductors can become less than the value calculated from this conductivity as space-charge boundary layers build up.

The conduction in insulators is represented by the same formula (equation 4) with K_G varying from less than 10^{-16} mho s/rad m in polystyrene and polyethylene to 10^{-12} mho s/rad m in pure single-crystal sapphire.² Polymers tend to have the lowest values and are followed in order by glasses, inorganic polycrystalline materials, and inorganic single-crystal materials.

There are also smaller delayed conductivity components that must be considered for some applications, particularly ones in which total charge conducted across an insulator is a relevant parameter.

2.3 Shield Currents

The AURORA test cell environment forces one to use shielded cables, so that large currents induced on conductors (from Compton replacement, electric field coupling, and magnetic field coupling) flow on the shields rather than on signal wires. Nevertheless, cable shields are imperfect and a fraction of the current can appear in the signal circuit. Typically, shield currents can range from 1 amp upward to several hundred amps, depending

on the location of the cable (cables laid close to metal surfaces and out of the direct ionization field will have the smaller currents).

The effect of shield currents on the signal response can be estimated using the cable transfer impedance, Z_T , the signal voltage per unit length per unit shield current. Typical values of Z_T for various types of cables versus frequency are shown in figure 1. For AURORA pulse shapes ($f \sim 4$ MHz) the transfer impedance of single-braid shield cables is $Z_T \sim 0.050$ ohm/m; for double-braid shield cables $Z_T \sim 0.001$ ohm/m. Therefore, the noise induced on a typical ~ 10 m single-braid shielded cable run from the test cell to the data room by ~ 1 amp of shield current is 500 mV. This noise can be decreased by surrounding the cable bundle by a solid metal shield. It can be significantly worse if the shield current is not led to a low-impedance ground, and is allowed to flow onto the oscilloscope chassis.

2.4 Photon-Induced Cable Current

Ionizing radiation induces currents into cables by Compton current transfer between the cable conductors and dielectric, and by conduction across air-filled gaps. Conduction is particularly serious, because in almost all cables small air-gaps exist (e.g., between shield wires and dielectric) and the gaps are pre-biased by charge trapped in the dielectric. Therefore, the magnitude and sign of the conduction are not accurately predictable.

The net effect on cables is a current source in the signal circuit described by

$$I = K_d \dot{D} . \quad (5)$$

Typical values of K_d are summarized in table 1. The smallest values are found in special "gapless" cables such as Aljac and Cujac. Next come solid dielectric cables (e.g., RG58, RG213). Cables with deliberate gaps (e.g.,

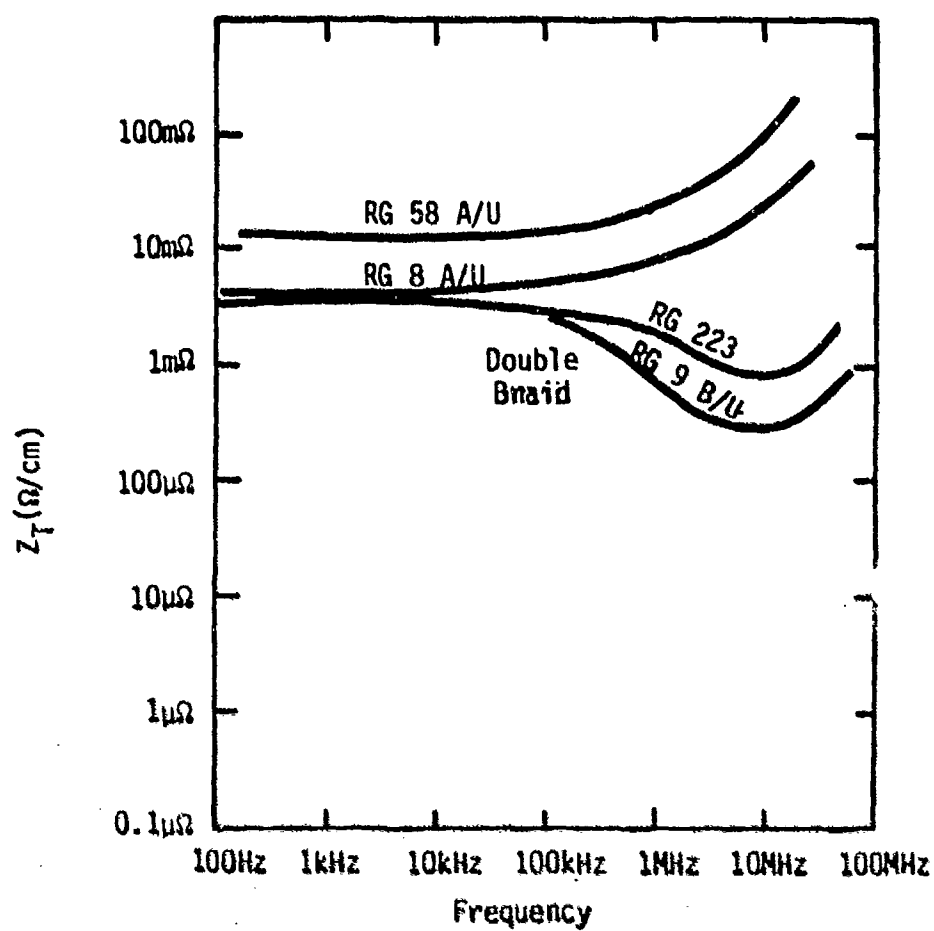


Figure 1. Comparison of Z_T values of various cables.¹

¹Ricketts, et al., EMP Radiation and Protective Techniques, John Wiley & Sons, 1976.

RG62) and foam dielectrics (e.g., RG331) exhibit the largest photon-induced currents.

Table 1. Typical Photon-Induced Cable Currents.

<u>Cable</u>	<u>K_d (C/rad-m)</u>	
RG-58	10^{-13}	
RG-11 (Triax)	$+10^{-13}$	
RG-213 (Coax)	$+10^{-12}$	
RG-59 (Coax)	$+10^{-12}$	
3/4" + 7/8"	10^{-11}	
Foam Coax		R57

For a typical AURORA application using RG58 ($K_d = 10^{-13}$ C/rad-m), a 1 m length of cable may be exposed at $\dot{D} = 10^{10}$ rads/s, followed by 10 m at 10^9 rads/s (e.g., in a trench). The net current induced in RG58 would be ~ 2 mA, creating a signal of ~ 100 mV across a 50Ω termination (assuming the source impedance is large compared to 50Ω).

3. ELECTRIC FIELD AND VOLTAGE MEASUREMENTS

3.1 Potential Difference Technique

The most common method of determining a vector component of the electric field is to measure the difference in potential between two electrodes. A limitation to this method is the degree to which the measuring circuit perturbs the field being measured. For fast response, electrostatic voltmeters cannot be used. Therefore, the measurement circuit draws current from the sensor. This current integrates to leave a net charge on the electrodes, changing the electric field between them. Furthermore, the electrodes, the associated wiring and signal-conditioning electronics introduce conductors that may perturb the field distribution.

To minimize the perturbation of the electric field by conductors requires that the sensor, the wiring, and the electronics metal surfaces be placed along equipotential surfaces. This implies that they must be small compared to the distance over which the electric field changes, and that the field direction is known. For this reason, electric field measurements are most readily performed next to flat conducting surfaces (e.g., the walls and floor of the AURORA screen room).

The effect of the measuring current on the field measurement can best be analyzed using the configuration shown schematically in figure 2a. The sensor electrodes have an area (A) and a spacing, d. They are connected to a series resistance (R_S) and a signal-conditioning amplifier with input resistance (R_A). If this sensor were subjected to a step function electric field (E), the voltage appearing at the amplifier input would be described by

$$V_{in} = \left(\frac{R_A}{R_A + R_S} \right) E \cdot d. \quad (6)$$

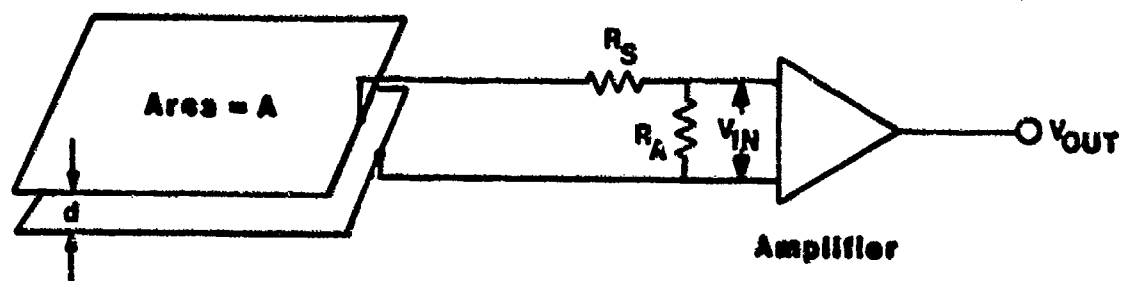
The current drawn from the sensors to establish this voltage is described by

$$I_{in} = \frac{E \cdot d}{R_A + R_S}. \quad (7)$$

As a result, the electrodes will accumulate charge and the electric field between them will be decreased. Eventually enough charge will accumulate on the electrodes to cancel the electric field between them. The characteristic charging time is described by

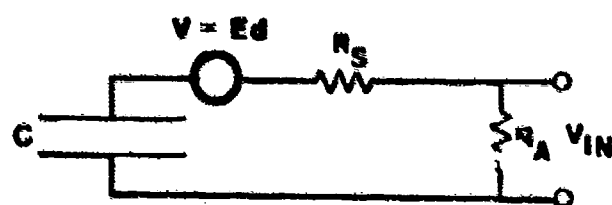
$$\tau = (R_A + R_S)C \quad (8)$$

where $C = \epsilon A/d$, and ϵ is the permittivity of the material between the electrodes. C equals the capacitance between the sensor electrodes. The equivalent circuit, shown in figure 2b, represents this response. As a result, the voltage sensitivity at the amplifier input can be expressed as



R57

a) Configuration.



b) Equivalent Circuit.

R57

Figure 2. Electric field sensor.

$$\frac{V_{in}}{E} = \frac{R_A A \epsilon}{\tau} e^{-t/\tau} \quad (9)$$

This relation illustrates the tradeoff between sensitivity and response time for such a sensor. The input resistance for the amplifier is limited by frequency response. Typically, for an amplifier input stray capacitance of C_A , the exponential rise time of the input signal is $\tau_r = R_A C_A$. Therefore, the input expression becomes

$$\frac{V_{in}}{E} = \frac{\tau_r}{\tau} \frac{A \epsilon}{C_A} e^{-t/\tau} \quad (10)$$

and the sensitivity is directly proportional to the quotient of rise time and fall time. For very fast rise times, the dimensions of the electrodes (e.g., their area A) is also limited because of signal propagation effects.

It should be noted that increasing the electrode spacing d , does not improve the sensitivity since the series resistor R_G has to be increased proportionately to preserve the low-frequency response. Increasing the electrode area can improve the sensitivity. This increased sensitivity is limited by the maximum dimension over which the electric field is uniform.

For a typical AURORA sensor,

$$\tau_r = 30 \text{ ns},$$

$$\tau = 5 \text{ } \mu\text{s},$$

$$A = 0.5 \text{ m}^2, \text{ and}$$

$$C_A = 30 \text{ pF}.$$

Therefore,

$$\frac{V_{in}}{E} \approx 10^{-3} \text{ m} \quad (11)$$

Also, if interference in the output cable is sufficiently small, R_S can be set equal to the cable characteristic impedance (e.g., 50Ω) and the amplifier eliminated. This results in reduced sensitivity with AURORA pulse widths. For the sensor described above,

$$\frac{V_{in}}{E} \cong 5 \times 10^{-5} \text{ m.} \quad (12)$$

Interferences result from radiation-induced Compton currents emitted from the electrodes, photon-induced cable currents in the input cable, and primary photocurrent in the input stage of the amplifier. If no amplifier is used, photon-induced cable current in the output cable also contributes significantly.

The Compton current from the electrodes charges the electrode capacitance, simulating a rate of change of E . The apparent rate of change is expressed by

$$\Delta \left(\frac{dE}{dt} \right) (\text{Compton}) = \frac{J_c A_w}{C} = \frac{J_c A_w d}{\epsilon A} \quad (13)$$

For this case we have assumed that a wire screen was used so that the area of the Compton-emitting solid, A_w , is less than the total area of the electrodes, A . If the resistor R_S is placed at the electrodes, the photon-induced current in the input cable produces a voltage across the amplifier input resistor, R_A , that adds to the primary photocurrent in the amplifier input stage. Therefore,

$$\Delta E (\text{Cable} + I_{pp}) = (K_d \dot{D} + K_{pp} \dot{D}) \frac{T}{AE} \quad (14)$$

For the above sensor, assume that the electrodes are screen (90 percent open area) of 0.1 g/cm^2 thick Al wire, that the Compton current imbalance between air and Al is approximately 10 percent, that the electrode spacing is 0.03 m , and that the dose rate at the sensor is $\dot{D} = 10^9 \text{ rads/s}$. Then

$$\Delta\left(\frac{dE}{dt}\right)(\text{Compton}) \approx \frac{2 \times 10^{-9} \times (1/3) \times 0.1 \times 0.03 \times 10^9}{9.9 \times 10^{-12}} \quad (15)$$

$$\approx 2 \times 10^8 \text{ V/m-s}.$$

At the end of a 10^{-7} s pulse accumulating a total dose of 10^2 rad, the error in E is 20 V/m. This error is approximately one percent of the fields created in the AURORA test cell. At higher dose rates the error can be significant.

Similarly, if one meter of RG58 cable (with $K_d = 10^{-13}$ C/rad-m) is illuminated by $\dot{D} = 10^9$ rads/s, and a preamp (with $K_{pp} = 10^{-12}$ C/rad) is exposed to 10^8 rads/s (in a shielded location), then

$$\Delta E(\text{Cable} + I_{pp}) \approx \frac{(10^{-13} \times 1 \times 10^9 + 10^{-12} \times 10^8) \times 3 \times 10^{-6}}{0.3 \times 9 \times 10^{-12}} \quad (16)$$

$$\approx 200 \text{ V/m}.$$

This interference is approximately 10 percent of the fields in the AURORA test cell.

3.2 Other Methods of Electric Field Measurement

A variety of other methods to measure the electric field have been considered, particularly for applications in which neither electrode can be at ground potential. The most promising appear to be the following methods.

1) Using electrodes and preamplifiers, such as those described in section 2.2, to drive a high frequency (~ 100 MHz) voltage-controlled oscillator (VCO) and a wide-band fiber-optics (FO) link. The FO link provides dielectric isolation, and the VCO overcomes the problem of transient fluorescence and darkening due to radiation exposure of the glass fibers.

2) Using a Pockels cell. A suitable crystal, located at the position at which the electric field is desired, is traversed by one to three polarized light beams. Up to three electric field components can be deduced from measurements of the rotation of the planes of polarization. The measurements can all be performed in a shielded location, with mirrors to guide the light beam(s). Effects of fluorescence in the air and crystal can be eliminated by using a narrow wavelength intense light source (e.g., a laser) and an interference filter at the receiver. The seriousness of transient darkening in the crystal needs to be investigated.

3.3 Voltage Measurement

The voltage between a point and ground can be measured using the method described in section 3.1. The key tradeoff is between the impedance with which the measuring point is loaded (i.e., $R_S + R_A$ must be sufficiently large compared to the source impedance of the voltage source), the response time (determined by R_A) and the input capacitance of the amplifier, and the sensitivity [which is proportional to $R_A / (R_A + R_S)$].

Interference is mostly from photon-induced cable currents and primary photocurrent in the input stage of the amplifier. For the same values used in section 2.2 (1 m of cable exposed to 10^9 rads/s, preamp exposed to 10^8 rads/s) the error in the measuring point voltage is given by

$$\Delta V = 2 \times 10^{-4} \frac{R_A + R_S}{R_A} \quad (17)$$

4. MEASUREMENTS OF MAGNETIC FIELDS AND CURRENTS

4.1 Magnetic Field Measurements

The most common method of determining a magnetic field in AURORA experiments is to measure the voltage developed in a wire loop by the rate

of change of magnetic field. The basic configuration is shown schematically in figure 3a. If we first neglect the magnetic field produced by the current flowing in the loop, the output voltage generated by a rate of change of magnetic field, B , is given by

$$V_o = A \cdot \dot{B} . \quad (18)$$

However, the output voltage produces a current $I = V_o/R$ across the load resistor, which in turn produces a flux linking the loop of LI (L is the loop inductance). Therefore, the output voltage, including the field produced by the current satisfies the equation

$$V_o = (A \cdot \dot{B}) - \tau \frac{dV_o}{dt} \quad (19)$$

where $\tau = L/R$. For a step function change in magnetic field (ΔB), the output is described by

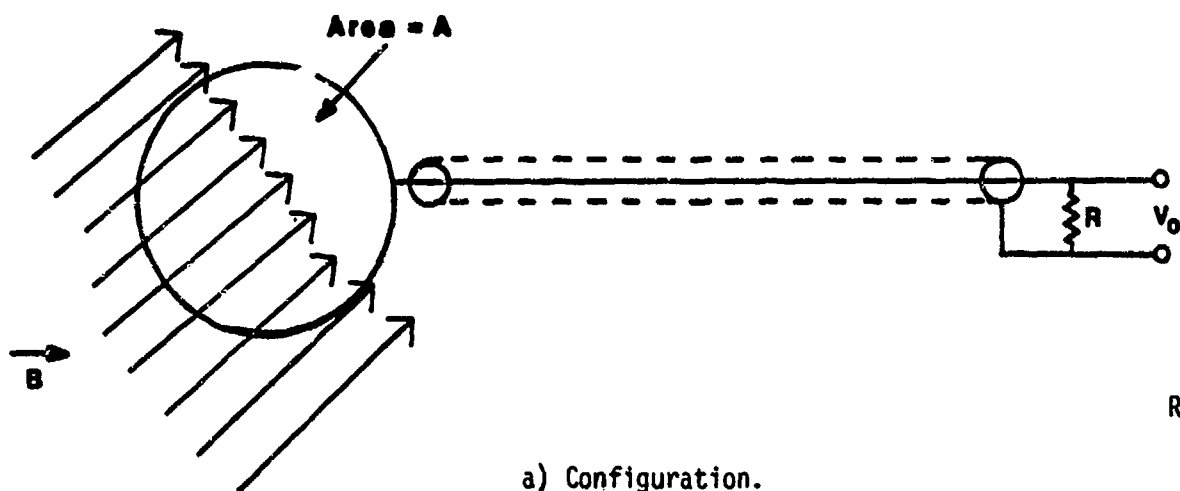
$$V_o = \frac{A \Delta B}{\tau} \exp(-t/\tau) . \quad (20)$$

For a long ramp at a rate \dot{B} , it is described by

$$V_o = A \cdot \dot{B} . \quad (21)$$

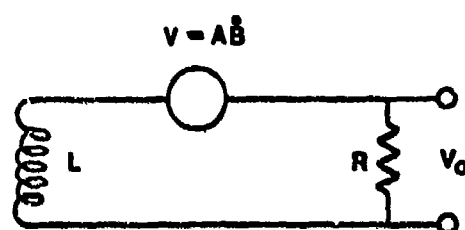
The equivalent circuit is shown in figure 3b. The equivalent circuit and the equations illustrate that, for magnetic fields changing on a time scale rapid compared to τ , the sensor output is $A \cdot \Delta B/\tau$. For changes on a time scale slow compared to τ , it is $A \cdot \dot{B}$. In other words, at high enough frequencies it changes from a \dot{B} to a B sensor and the transition frequency is determined by $\omega \approx 1/\tau = R/L$.

The sensor loop illustrated in figure 3a has the shortcoming that it also responds to a changing electric field. When the electric field changes, charge must move through the loop inductance to restore the wire to its previous voltage. An effective method to decrease the E-field sensitivity



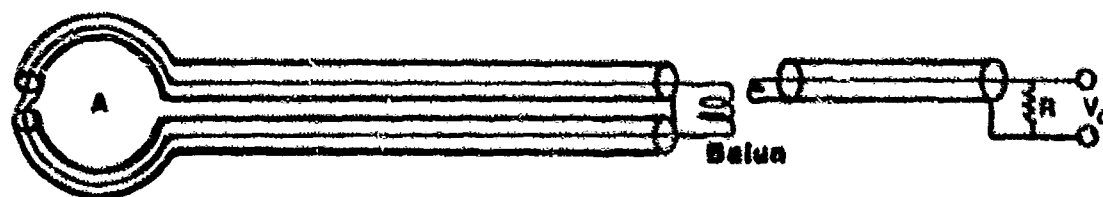
R57

a) Configuration.



b) Equivalent circuit.

R57



c) Mobius loop configuration.

R57

Figure 3. Magnetic field sensor.

and at the same time decrease the radiation response, is to use a balanced Mobius loop (shown in figure 3c). Two coax cable half loops are joined at their ends by connecting each center conductor to the other's shield. The symmetry of this arrangement is preserved by passing the signal through a balun transformer before connecting to a single-ended recording device. Tracing the circuit shows that there are effectively two turns around the loop area A. This gives the sensor twice the sensitivity of the single turn device of figure 3a (and also twice the self inductance).

For a typical AURORA sensor with an effective loop area (A) of $3 \times 10^{-2} \text{ m}^2$ and a self inductance (L) of $1 \text{ } \mu\text{H}$, driving a terminated 50 ohm cable, the sensitivity is expressed as

$$V_o(V) = 3 \times 10^{-2} \dot{B}(\text{Weber/m}^2 \text{ s})(\text{A/m-s}) \quad (22)$$

and the effective sensor integration time is 20 ns.

The potential interference effects are due to ionization-induced conduction in the cable insulator and insulator at the Mobius loop crossover, and photon-induced cable currents. Assuming the insulator thicknesses are $\sim 10^{-3} \text{ m}$, the effective shunt resistance produced in $\sim 10 \text{ m}$ of cable exposed at 10^9 rads/s of insulator with $K_G = 10^{-16} \text{ mho s/rad m}$ is $\sim 10^5 \text{ Ohm}$. This is very large compared to the 50 ohm cable terminator. If we assume that the balanced geometry cancels all but ten percent of the photon-induced cable current, the net effect of a dose rate \dot{D} on a length, L , of cable is to place an additional current source in series with the voltage source with an amplitude of $0.1 K_G \dot{D} A$ (see figure 3b). For a photon pulse rise time slow compared to L/R , the resultant output interference voltage looks like a derivative of the radiation pulse, with amplitude described approximately by

$$\Delta V \approx 0.1 K_G \dot{D} L. \quad (23)$$

For an exposure of 10 m of RG58 to a dose rate of 10^9 rads/s rising in 50 ns and a sensor inductance of 1 μ H, this becomes 2 mV. The equivalent error in magnetic field accumulated by the time the dose rate achieves D is described approximately by

$$\Delta B \approx 0.1 K_d \dot{D} L / A . \quad (24)$$

For the sample problem above, the error in magnetic field is 3×10^{-9} Weber/m². This is very small compared to the magnetic fields at AURORA.

4.2 Surface Current Measurement

Measurement of surface current density (J_s) follows directly from the magnetic field measurement described in section 4.1. The magnetic field near the surface is related to the surface current by

$$B_x = \mu_0 J_{sy} \quad (25)$$

where $\mu_0 = 4\pi \times 10^{-7}$ H/m, the permeability of space. Therefore a sensor of the type discussed in section 4.1, usually in the form of a semicircle with its axis in the plane of the surface, measures the rate of change of surface current. Thus, for rise times slow compared to $\tau = L/R$,

$$V_o = \mu_0 A \dot{J}_s . \quad (26)$$

The interference terms are similar to those discussed in section 4.1

For a sensor with half the area and inductance as the example in section 4.1

$$V_o(V) = 2 \times 10^{-8} \dot{J}_s (A/m-s) \quad (27)$$

and the interference at $\dot{D} = 10^9$ rads/s is

$$\Delta J_s = 3 \times 10^{-3} \text{ A/m} . \quad (28)$$

4.3 Volume Current Density

The net current density in a small volume in the AURORA test cell is determined by measuring the magnetic flux linking a loop under controlled boundary conditions. The geometry is illustrated in figure 4. A conducting cylinder of radius, a , and length, ℓ , is placed with its axis parallel to the current flow, J_v , to be measured. A Mobius loop \dot{B} detector (two turns) is placed with one edge along the cylinder's axis, and the remaining edges along radii at the ends and along the side wall. By symmetry, the azimuthal magnetic field as a function of radius, r , is described by

$$B_\phi = \frac{\mu_0 J_v r}{2} . \quad (29)$$

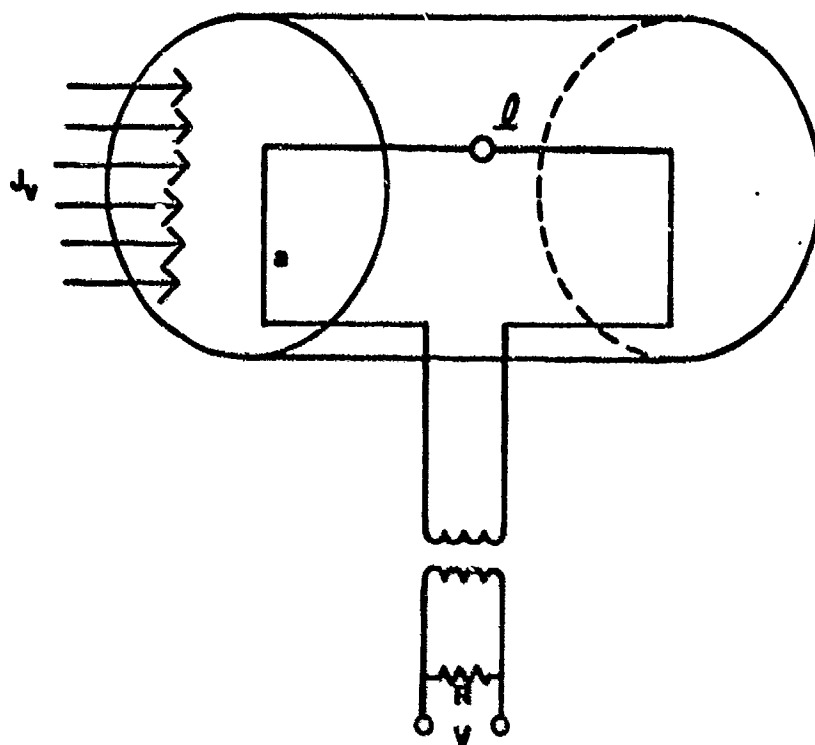
The sensitivity, for J_v varying slowly compared to L/R , is described by

$$V = \frac{1}{2} \mu_0 a^2 \ell \frac{dJ_v}{dt} . \quad (30)$$

The dominant interference terms are again photon-induced cable currents and electron transfer to and from the cable shields, both of which are partially cancelled by the symmetric Mobius loop configuration. In effect, these currents produce an additional signal by the voltage they develop across the loop inductance. Thus, the interference signal is described by

$$V = [f_L k_C (2\ell + a)d + f_C k_d \ell_C] L \dot{D} \quad (31)$$

where f_L is the fraction of the Compton current incident on the wire loop, f_C is the fraction of the photon-induced cable current producing an imbalanced signal, d is the thickness of the loop wire, and ℓ_C is the length of cable



R57

Figure 4. Volume current density sensor.

exposed to radiation. As a result, an error in the measured volume current is described by

$$\Delta J_V = \frac{2[f_\ell K_C(2\ell+a)d + f_c K_d \ell_c] L \dot{D}}{\mu_0 a^2 \ell} \quad (32)$$

A typical AURORA sensor has dimensions of $\ell = 0.5$ m, $a = 0.25$ m, $d = 10^{-3}$ m, and $L = 4$ μ H. The sensitivity is $V(V) = 2 \times 10^{-8}$ dJ_V/dt (A/m²·s). If we assume $f_\ell = f_c = 0.1$, $\ell_c = 10$ m, and using $K_C = 2 \times 10^{-8}$ C/rad m², the interference at $\dot{D} = 10^9$ rads/s is

$$\Delta J_V = 0.7 \text{ A/m}^2. \quad (33)$$

This compares favorably with the volume Compton current of $J_V = 20 \text{ A/m}^2$ produced by the same 10^9 rads/s interacting with the air.

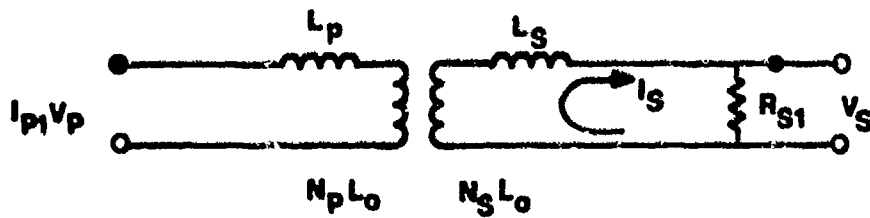
4.4 Measurement Of Current In A Conductor

4.4.1 Current Probe

The usual method of measuring the current in a conductor (e.g., wire, strut) is to use a ferrite-core current transformer. The conductor is passed through the core (i.e., one-turn primary) and the voltage induced in a secondary winding is measured. The equivalent circuit for such a current probe is shown in figure 5a. We assume a primary leakage inductance of L_p , a mutual inductance of $N_p N_s L_0$, and secondary leakage inductance of L_s . We will first neglect the leakage inductances L_p and L_s . The response to a rapid change in primary current I_p , is to produce a secondary current given by

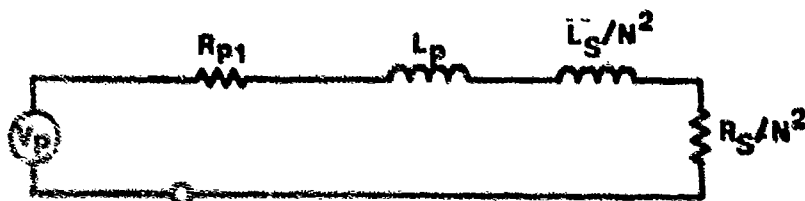
$$I_S = \frac{N_p}{N_s} I_P = \frac{1}{N} I_P \quad (34)$$

where $N = N_s/N_p$ is the turns ratio. To drive this current through the



R57

a) Equivalent circuit.



b) Reflection in primary.

R57

Figure 5. Current probe.

resistor, a secondary voltage of

$$V_S = I_S R_S \quad (35)$$

is required. To sustain this secondary voltage, the net flux in the core must build up at the rate

$$N_S \frac{d\phi}{dt} = I_S R_S = N_S^2 L_0 \frac{dI_S}{dt} \quad (36)$$

Therefore, the secondary voltage will decay according to the relationship

$$V_S(t) = \frac{I_P R_S}{N} e^{-t/\tau_d} \quad (37)$$

where $\tau_d = N_S^2 L_0 / R_S$. Similarly, the voltage reflected into the primary to sustain the constant primary current is given by

$$V_P = \frac{V_S}{N} = \frac{I_P R_S}{N^2} e^{-t/\tau_d} \quad (38)$$

If the input current is sustained, the magnetic flux may build up to the saturation flux density, ϕ_{Sat} . This will occur when

$$\phi_{Sat} = \int \frac{d\phi}{dt} dt = \frac{1}{N_S} \int V_S dt \quad (39)$$

Therefore, saturation can be expressed as a voltage-time product for the secondary circuit. Equivalently, for the primary circuit

$$\phi_{Sat} = \frac{1}{N_P} \int V_P dt \quad (40)$$

If core saturation is a problem, it is best solved by current dividing so that only a fraction of the current passes through the probe. Care must be taken to ensure that the probe insertion impedance is small compared to the divider impedance.

The leakage inductances limit the high frequency response of the current probe by introducing an additional reactive impedance in series with the primary and secondary circuits. This can be seen in figure 5b, which illustrates the equivalent circuit as reflected in the primary circuit with a Thevenin equivalent source attached. If the current probe is not to perturb the current being measured, R_S/N^2 should be small compared to R_p . The effective rise time of current in the circuit can then be expressed as

$$\tau_R = [L_p + (L_S/N^2)]/R_p \approx L_1/R_p \quad (41)$$

where L_1 is the insertion inductance.

Interference in current probes is principally from imbalanced charge transfer in the probe and photon-induced cable currents. This is best represented as an additional current in the secondary current, ΔI_S . If we assume the primary circuit is truly a current source (i.e., high impedance), all of the extra current must flow through the resistor R_S , producing an error voltage $\Delta V_S = R_S \Delta I_S$. This could be interpreted as an erroneous primary circuit current given by

$$\Delta I_p = N \Delta I_S \quad (42)$$

If the primary circuit has a finite impedance of R_p , the extra current will be shared between R_S and R_p/N^2 . This will produce extra current in the primary circuit and a smaller error in the interpreted current.

Examples of current probes used at AURORA are the Tektronix Models CT-1, CT-2, and Singer 94106-1. Their characteristics are summarized in table 2.

Table 2. Current Probe Specifications.

	Tektronix CI-1	Tektronix CI-2	Singer 94106-1	Pearson 2100
Sensitivity (V/A)	5	1	1	1
Insertion Resistance (Ohm)	1	.04	.04	.02
Insertion Inductance (μ H/t)	5	5		
Output Saturation Characteristic (Output V μ s)	5	50	$>10^5$	5000
Secondary Decay Time (μ s)	5	125	10	1500

4.4.2 Series Resistor

Another method of measuring a current is to convert it into a voltage by inserting a series resistor. This technique is useful in low-current high-impedance circuits where large series resistors (i.e., >10 Ohm) are acceptable. Unless long-term response is needed (i.e., times longer than $N_S^2 L_0 / R_S$) a current probe is more convenient for modest-current applications.

5. MEASUREMENT OF AIR CONDUCTIVITY

5.1 Parallel Plate Ionization Chamber

The conductivity of ionized air as a function of electric field is a fundamental parameter determining the net electric and magnetic fields in an ionized air volume. The simplest measuring device is a parallel plate ionization chamber, otherwise known as a "pie-pan". A version used for careful measurements of the attachment rate α , and mobility μ , in air is shown in figure 6. The double-sided geometry and radiation collimators are used to minimize the effects of Compton transfer currents on the conductivity measurement*.

An ionization pulse produces electron-ion pairs at a rate of

$$\frac{dn}{dt} = K_g P \dot{D} \quad (43)$$

where $K_g = 2.2 \times 10^9$ in air at 293°K, and P is the pressure in atmospheres. The electrons are removed by attachment at the rate of αn ; they drift under the influence of an electric field, E , at a velocity μE . We will neglect the effect of density gradients on the electron transport. We will also neglect the motion of positive and negative ions, since the ion mobility is small compared to the electron mobility.

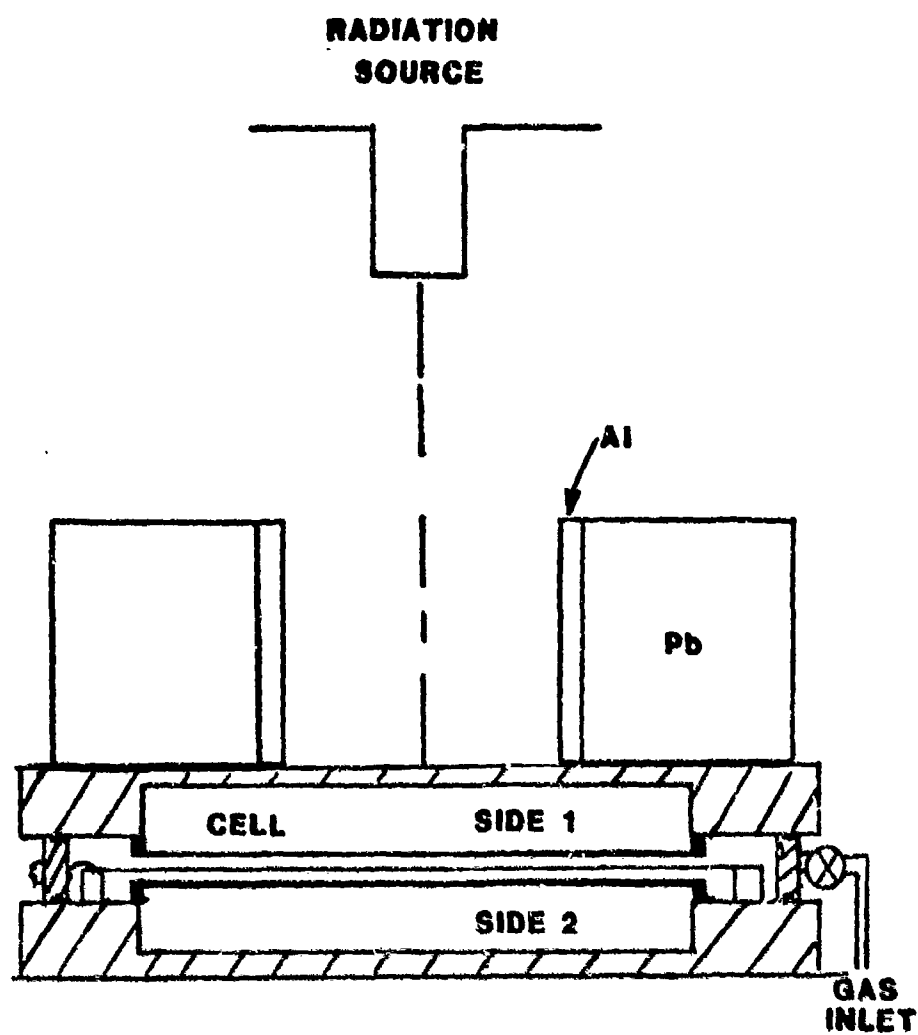


Figure 6. Schematic diagram of the "pie pan" experiment.

Consider first that a density of K_g PD electrons are generated in a pulse short compared to the attachment and sweep-out times. Attachment and drift in an ion chamber with two sides, gap width, a , exposed area, A , under an electric field, E , produces an external circuit current of

$$I(t) = 2e_0 \mu E A K_g P D e^{-\alpha t (1 - \mu E t / a)} \quad (44)$$

If the dose, D , is calibrated, the mobility can be calculated from the peak current at $t=0$ (before attachment or sweep-out). Given the mobility, a sweep-out correction for the last factor can be performed and the remaining current decay fitted to an exponential with a slope of $1/\alpha$.

At higher pressures, the attachment time, $1/\alpha$, is comparable to the ionization pulse width and the foregoing procedure does not work. In this case the sweep-out correction $(1 - \mu E t / a)$ is almost always indistinguishable from unity and we can use the total charge collected, $Q = \int_0^\infty I dt$ to calculate (μ/α) . Therefore,

$$Q = \int_0^\infty I dt = 2e_0 E A K_g P D (\mu/\alpha) \quad (45)$$

and
$$(\mu/\alpha) = \frac{Q}{2e_0 E A K_g P D} \quad (46)$$

There are serious limitations to the use of such ion chambers. They are:

- 1) At low electric fields the conduction current is masked by net Compton transfer currents and photon-induced cable currents. With careful collimation and shielding, measurements in air at 0.6 atm pressure were performed at NIFX down to an applied voltage of 7 V/cm.¹
- 2) At high electric fields and high doses the boundary layer of positive charge near the anode (from which the electrons have been removed by drifting) can absorb a significant fraction of the applied voltage. This process decreases the electric field where the electrons are still drifting. The magnitude of the change in electric field can be expressed approximately as

$$\frac{E(t)}{E} = \frac{e_0 K_g P D \mu^2 E}{\epsilon_0 a} \{1 - e^{-\alpha t} - \alpha t e^{-\alpha t}\} . \quad (47)$$

When most electrons are attached rather than swept out, the asymptotic value is expressed as

$$\frac{E(\infty)}{E} = \frac{e_0 K_g P D \mu E}{\epsilon_0 a} (\mu/\alpha)^2 . \quad (48)$$

This formula illustrates that the fractional change in electric field increases with increasing electric field.

5.2 Microwave Absorption And Scattering

Microwave transmission is an effective means of measuring air conductivity. At a microwave angular frequency, ω , the complex conductivity, $\tilde{\sigma}$, of a gas containing an electron density, n , that undergo momentum transfer collisions at a rate, g , is described by

$$\tilde{\sigma} = \frac{n e_0^2}{M_0 \omega} \frac{(g/\omega) + i}{1 + g^2/\omega^2} . \quad (49)$$

where M_0 is the electron mass. The real and imaginary portions of the conductivity can be deduced from the attenuation and phase shift of a microwave beam passing through the ionized gas. For example, in a waveguide of transverse dimensions (a,b) excited by a TE_{01} mode, the propagation constant in the ionized medium is $i\Gamma + \tilde{\gamma}$, where

$$i\Gamma = i(\omega^2/c^2 - \pi^2/a^2)^{1/2} \quad (50)$$

is the expression for the propagation constant in the waveguide without air conductivity, and

$$\tilde{\gamma} = i[-\Gamma^2 + (\tilde{\Gamma}^2 - i\omega\mu\tilde{\sigma})^{1/2}] \quad (51)$$

describes the change introduced by the conductivity.

The complex amplitude, \tilde{A} , relative to the value without conductivity, after propagating down a uniformly ionized section of waveguide of length L can be calculated as a straightforward boundary value problem:

$$\tilde{A} = \exp(-\tilde{\gamma}L) \left[1 - \frac{\tilde{\gamma}^2}{4\Gamma^2(1-i\tilde{\gamma}/\Gamma)} [1 - \exp(-2i\Gamma L - 2\tilde{\gamma}L)] \right] \quad (52)$$

This attenuation and phase shift of the microwave beam can be deduced from measurements with a microwave bridge.¹ Electron densities down to 10^{15} m^{-3} can be measured with this method.

More sensitive techniques use microwave cavities. These are not as easily calibrated as a waveguide, but can detect electron densities smaller by factors of 10^3 or more. Some of these are summarized in reference 4.

REFERENCES

1. M. L. Price, V. A. J. van Lint, Measurement of Electron Attachment and Mobility in Dry and Wet Air, DNA 4788T, Mission Research Corporation, December 1978.
2. T. J. Ahrens and F. Wooten, "Electrical Conductivity Induced In Insulators by Pulsed Radiation," IEEE Trans. Nucl. Sci., NS-23, No. 6, 1268 (1976).
3. J. G. Chervenak, et al., "Photon-Induced Anomalous Cable Currents," IEEE Trans. Nucl. Sci., NS-26, No. 6, 4927, December 1979.
4. V. A. J. van Lint, J. Perez, D. Trueblood, M. E. Wyatt, "Techniques for Studying Electrons During Ionization Afterglows," Rev. Sci. Inst., 36, 521 (1965).

DISTRIBUTION

ASSISTANT TO THE SECRETARY OF DEFENSE
ATOMIC ENERGY
ATTN MILITARY APPLICATIONS
ATTN EXECUTIVE ASSISTANT
WASHINGTON, DC 20301

DIRECTOR
DEFENSE COMMUNICATIONS AGENCY
ATTN CODE 312
ATTN CODE C313
ATTN CODE 430, PARKER
WASHINGTON, DC 20305

DEFENSE COMMUNICATIONS ENGINEER CENTER
1860 WIEHLE AVE
ATTN CODE R400
ATTN CODE R123, TECH LIB
RESTON, VA 22090

DIRECTOR
DEFENSE INTELLIGENCE AGENCY
ATTN DB 4C2, D. SPOHN
ATTN RTS-2A, TECH LIB
WASHINGTON, DC 20301

DIRECTOR
DEFENSE NUCLEAR AGENCY
ATTN NATA
ATTN TITL (4 COPIES)
ATTN RAEV
ATTN RAE, G. BAKER (10 COPIES)
ATTN STNA
WASHINGTON, DC 20305

ADMINISTRATOR
DEFENSE TECHNICAL INFORMATION CENTER
ATTN DTIC-DDA (12 COPIES)
CAMERON STATION
ALEXANDRIA, VA 22314

JOINT CHIEFS OF STAFF
ATTN J-3 RM 2D874
WASHINGTON, DC 20301

NATIONAL COMMUNICATIONS SYSTEM
OFFICE OF THE MANAGER
DEPARTMENT OF DEFENSE
ATTN NCS-TS
WASHINGTON, DC 20305

DIRECTOR
NATIONAL SECURITY AGENCY
ATTN TDL
ATTN R-52, O. VAN GUNTEN
ATTN S-232, D. VINCENT
FT GEORGE G. MEADE, MD 20755

COMMANDER
BMD SYSTEMS COMMAND
DEPARTMENT OF THE ARMY
ATTN BMDSC-AOLIB
ATTN BMDSC-HLE, R. WEBB
PO BOX 1500
HUNTSVILLE, AL 35807

DIVISION ENGINEER
US ARMY ENGR. DIV. HUNTSVILLE
ATTN T. BOLT
PO BOX 1600, WEST STATION
HUNTSVILLE, AL 35807

DIRECTOR
US ARMY BALLISTIC RESEARCH LABS
ATTN DRDAR-BLB, W. VAN ANTWERP
ATTN DRDAR-BLE
ABERDEEN PROVING GROUND, MD 21005

COMMANDER
US ARMY COMMUNICATIONS COMMAND
ATTN CC-LOG-LEO
ATTN CC-OPS-WS, CONNELL
ATTN CC-OPS-PD
ATTN CC-OPS-OS
ATTN ATSI-CD-MD
FT HUACHUCA, AZ 85613

CHIEF
US ARMY COMMUNICATIONS SYS AGENCY
DEPARTMENT OF THE ARMY
ATTN CCM-AD-SV
ATTN CCM-RD-T
FT MONMOUTH, NJ 07703

COMMANDER
US ARMY NUCLEAR & CHEMICAL AGENCY
ATTN NONA-WE
ATTN DR. BERBERET
7500 BACKLICK ROAD
BUILDING 2073
SPRINGFIELD, VA 22150

DISTRIBUTION (Cont'd)

COMMANDER
US ARMY TRAINING AND DOCTRINE COMMAND
ATTN ATCD-Z
FT MONROE, VA 23651

BMD CORP
ATTN CORPORATE LIBRARY
7915 JONES BRANCH DRIVE
MCLEAN, VA 22101

BENDIX CORP
COMMUNICATION DIVISION
ATTN DOCUMENT CONTROL
E JOPPA ROAD
BALTIMORE, MD 21204

DIKEWOOD CORPORATION
ATTN TECHNICAL LIBRARY
1613 UNIVERSITY BLVD, NE
ALBUQUERQUE, NM 87102

ELECTRO-MAGNETIC APPLICATIONS, INC.
ATTN D. MEREWETHER
PO BOX 8482
ALBUQUERQUE, NM 87198

GENERAL ELECTRIC CO.
SPACE DIVISION
VALLEY FORGE SPACE CENTER
ATTN J. ANDREWS
PO BOX 8555
PHILADELPHIA, PA 19101

GTE/SYLVANIA
ATTN J. KILLIAN
1 RESEARCH DRIVE
WESTBORO, MA 01581

HONEYWELL, INC.
AEROSPACE & DEFENSE GROUP
ATTN S. GRAFF
ATTN W. STEWART
13350 US HIGHWAY 19 SOUTH
CLEARWATER, FL 33516

IIT RESEARCH INSTITUTE
ELECTROMAG COMPATIBILITY ANAL CTR
ATTN ACOAT
N SEVERN
ANNAPOLIS, MD 21402

IIT RESEARCH INSTITUTE
ATTN I. MINDEL
10 W 35TH ST
CHICAGO, IL 60616

IRT CORP.
ATTN J. KNIGHTON
PO BOX 81087
SAN DIEGO, CA 92138

LUTECH, INC.
ATTN F. TESCHE
PO BOX 1263
BERKELEY, CA 94701

MARTIN MARIETTA CORP
ATTN M. GRIFFITH (2 COPIES)
ATTN J. CASALESE
ATTN B. BROULIK
PO BOX 5837
ORLANDO, FL 32855

MCDONNELL DOUGLAS CORP
ATTN S. SCHNEIDER
ATTN TECHNICAL LIBRARY SERVICES
5301 BOLSA AVE
HUNTINGTON BEACH, CA 92647

MISSION RESEARCH CORPORATION
ATTN J. RAYMOND
ATTN J. CHERVENAK
5434 RUFFIN ROAD
SAN DIEGO, CA 92123

MISSION RESEARCH CORP
ATTN W. CREVIER
ATTN C. LONGMIRE
ATTN EMP GROUP
PO DRAWER 719
SANTA BARBARA, CA 93102

MISSION RESEARCH CORPORATION
ATTN W. STARK
ATTN J. LUBELL
ATTN W. WARE
PO BOX 7816
COLORADO SPRINGS, CO 80933

RICHARD L. MONROE ASSOCIATES
1911 R STREET NW
SUITE 203
WASHINGTON, DC 20009

DISTRIBUTION (Cont'd)

NORTHROP CORP.
ELECTRONIC DIVISION
ATTN LEW SMITH
ATTN RAD EFFECTS GRP
ATTN B. AHLPORT
2301 W 120TH ST
HAWTHORNE, CA 90250

R&D ASSOCIATES
ATTN DOCUMENT CONTROL
ATTN W. GRAHAM
ATTN C. MO
ATTN M. GROVER
PO BOX 9695
MARINA DEL REY, CA 90291

RAYTHEON CO
ATTN G. JOSHI
ATTN H. FLESCHER
HARTWELL ROAD
BEDFORD, MA 01730

ROCKWELL INTERNATIONAL
ATTN B-1 DIV TIC (BAOB)
PO BOX 92098
LOS ANGELES, CA 90009

SEA
MARINER SQUARE
ATTN W. HUTCHINSON
SUITE 127
1900 N. NORTHLAKE WAY
PO BOX 31819
SEATTLE, WA 98103

SRI INTERNATIONAL
ATTN E. VANCE
ATTN A. WHITSON
333 RAVENSWOOD AVE
MENLO PARK, CA 94025

TELEDYNE-BROWN ENGINEERING
ATTN O. GUICE
CUMMINGS RESEARCH PARK
HUNTSVILLE, AL 35807

TRW ELECTRONICS AND DEFENSE SYSTEMS GROUP
ATTN W. GARGARO
ATTN L. MAGNOLIA
ATTN R. PLEBUCH
ATTN C. ADAMS
ATTN H. HOLLOWAY
ATTN E. HORGAN
ATTN J. PENAR
ONE SPACE PARK
REDONDO BEACH, CA 90278

HARRY DIAMOND LABORATORIES
ATTN CO/TD/TSO/DIVISION DIRECTORS
ATTN RECORD COPY, 81200
ATTN HDL LIBRARY, 81100 (3 COPIES)
ATTN HDL LIBRARY, 81100 (WOODBIDGE)
ATTN TECHNICAL REPORTS BRANCH, 81300
ATTN CHAIRMAN, EDITORIAL COMMITTEE
ATTN LEGAL OFFICE, 97000
ATTN BRANCH 20000
ATTN BRANCH 20240 (10 COPIES)
ATTN BRANCH 21100
ATTN BRANCH 21200
ATTN BRANCH 21300 (10 COPIES)
ATTN BRANCH 21400
ATTN BRANCH 21500
ATTN BRANCH 21000
ATTN BRANCH 22000
ATTN BRANCH 22300 (2 COPIES)
2800 POWDER MILL RD
ADELPHI, MD 20783